Multi-source Perturbations in the Evolution of a Low-latitudinal Equatorial Plasma Bubble Event Occurred over China

Longchang Sun[1], Jiyao Xu[1, 2], Yajun Zhu[1, 2], Wei Yuan[1], and Chunxiao Yan[1]

[1]State Key Laboratory of Space Weather, National Space Science Center, Chinese Academy of Sciences, Beijing 100190, China;

[2]University of Chinese Academy of Sciences, Beijing 100049, China;

[3]Key Laboratory of Earth and Planetary Physics, Institute of Geology and Geophysics, Chinese Academy of Sciences, Beijing 100029, China

Correspondence to: J. Y. Xu, xujy@nssc.ac.cn

Key points:

1. Post-sunset bifurcated/plume-like structures with faster poleward/upward velocities evolved from bottom-type structures by PRE-inducing RTI
2. An equatorward wind-inducing RTI forced topside structures of developed depletions to form secondary bifurcated/plume-like ones near midnight
3. Cluster-type depletions were modulated by an LSWS occurring on the bottomside of the ionosphere

Abstract:

In this paper, multi-ground-based instruments, including an all-sky airglow imager (ASAI), a very high frequency (VHF) radar, and eight digisondes, were combined to investigate multi-source perturbations in the evolution of an EPB event that occurred over low latitudes in China. We found this EPB event initially evolved from the bottom-type structures, most likely seeded by the atmospheric gravity wave (AGW) and the collisional shear-type instability (CSI)-inducing perturbations. Once formed, those bottom-type structures further evolved into bifurcated/plume-like structures at the ionospheric topside by the generalized Rayleigh-Taylor instability (RTI). Observed and analyzed are two different perturbation mechanisms of RTIs: one is the prereversal enhancement of the zonal electric field (PRE) inducing-RTI; another is the equatorward wind-inducing RTI around midnight. Accompanied by the PRE-inducing RTI are bifurcated/plume-like structures with a larger poleward (upward) velocity. The PRE could directly elevate the bottom-type structures to the ionospheric topside

where the bifurcated/plume-like structures were generated by the RTI process. The near-midnight RTI was trigged by a vertical upward plasma jet caused by a seasonal equatorward wind in a region far away 10 ℃N (20 ℃N) from the geomagnetic (geographic) equator. This equatorward wind-inducing RTI persistently forced topside structures of those developed depletions to form secondary bifurcated/plume-like structures near midnight. Poleward developments of two cluster-type depletions of the EPB event were modulated by a large-scale wave-like structure (LSWS) occurring on the bottomside of the ionosphere. An eastward/westward polarization electric field inside the upwelling/trough region of the LSWS could accelerate/suppress the development of cluster-type depletions.

Plain Language Summary

Observational evidence is insufficient to understand how equatorial plasma bubbles (EPBs) form over low latitudes. The perturbation sources of EPBs are various and in dispute. This paper highlights the significance of multi-source perturbations in the evolution of a low-latitudinal EPB event in China. We found both the atmospheric wave (AGW) and the collisional shear-type instability (CSI)-inducing bottom-type structures likely seed the EPB event; those bottom-type perturbations further evolved into the bifurcated/plume-like structures by the generalized Rayleigh-Taylor instability (RTI) at the ionospheric topside. The prereversal enhancement of the zonal electric field (PRE)-driving RTI process well explain those post-sunset bifurcated/plume-like structures with faster poleward/upward velocities than those bifurcated/plume-like structures near-midnight excited by a seasonal equatorward wind-inducing RTI process. Meanwhile, those EPB depletions were modulated by a large-scale wave-like structure (LSWS) occurring on the ionospheric bottomside.

1. Introduction

There are equatorial plasma bubbles (EPBs), a nighttime phenomenon that frequently occurs in the low-latitudinal ionosphere. They manifest themselves as the field-aligned depleted regions of airglow intensity in optical observations (e.g., Kelley et al., 2002), bite-out structures in satellite observations (e.g., Weber et al., 1982), and plume-like structures in radar observations (e.g., Tsunoda et al., 1982). Since these EPBs can cause severe outages in satellite-based communication and navigation systems, understanding the day-to-day variability of this phenomenon is one of the important topics of space weather interest.

Observations (e.g., Huang, Burke et al. 2001; Burke et al. 2004) indicate that EPBs frequently occur at post-sunset when the ionosphere is significantly uplifted by a prereversal enhancement of the zonal electric field (PRE; Fejer et al., 1991; 1999). The sunset PRE can trigger the generalized Rayleigh-Taylor instability (RTI), which

is the dominant driving mechanism of EPBs (Kelley, 1989). However, this mechanism cannot explain the wave-like depletions with a typical wavelength of 400-1000 km, the cluster-type depletions with a smaller spacing (~100 km), and the freshly-generated depletions of EPBs near midnight. Thus, rather than the PRE, other seeding perturbations on the ionosphere bottomside can also initialize EPBs by the RTI process.

One of the most invoked seeding perturbations for EPBs is the atmospheric gravity wave (AGW), which well explains the periodic characteristic of the successive EPB depletions (e.g., Makela et al., 2010; Takahashi et al., 2009; 2010). Freely propagating secondary AGWs with wavelengths higher than 150 km in the thermosphere (Vadas, 2007) can seed EPBs. Pieces of observation evidence (e.g., Tsunoda et al., 1982; Makela & Miller, 2008; Thampi et al., 2009; Narayanan et al., 2012) indicates that a large-scale wave-like structure (LSWS) can also initialize EPBs from its upwelling regions. An LSWS can appear well before *E* region sunset (Tsunoda et al., 2010; Thampi et al., 2009), playing a more dominant role in the development of EPBs than the post-sunset rise (PSSR) of the *F*-layer, and causing the day-to-day variation of EPBs (Tsunoda, 2005). However, observations (e.g., Makela & Miller, 2008; Narayanan et al., 2012) indicated that the LSWS is not sufficient to explain those cluster-type depletions (typical scale ~100 km) inside the upwelling regions of an LSWS. It is promising that either the gradient drifting-type instability (Kelley, 1989) or the collisional shear-type instability (Hysell & Kudeki., 2004) occurring on the ionospheric bottomside explains those cluster-type depletions. However, evidence for perturbations caused by such ionospheric instability is lacking.

Besides, evidence (e.g., Miller et al., 2009; Abdu et al., 2003; Abdu, 2012; Wu et al., 2020) also indicates that electric field-inducing perturbations can be the seeding of EPBs. Intrinsic polarization electric fields (PEF) inside nighttime electrical medium-scale traveling ionospheric disturbances (EMSTIDs) can also initialize EPBs occurred near midnight (e.g., Miller et al., 2009). However, since EMSTIDs almost occur in the nighttime of the autumn and winter solstices (Garcia et al., 2000; Candido et al., 2008; Martinis et al., 2010; Huang, Dou et al., 2016; Shiokawa, et al., 2003; Xu et al., 2021), the EMSTIDs inducing-PEF cannot explain those EPBs occurring at equinoxes. Disturbed dynamo electric fields with the same polarity as the sunset PRE in the coupling of solar wind and magnetosphere can also contribute to the generation of nighttime EPBs (e.g., Abdu et al., 2003; Abdu, 2012; Wu et al., 2020). However, this mechanism cannot explain most EPBs frequently occur during geomagnetically quiet times.

Few studies (e.g., Yokoyama et al., 2011; Ajith et al., 2016; Dao et al., 2016, 2017; Sun et al., 2021a) found an equatorward neutral wind (ENW) can also initialize EPBs, especially those near midnight. Those studies suggested that the uplift of the ionosphere by an ENW could cause a decreasing ion-neutral collision frequency, resulting in an increasing gravity-driven eastward electric current that can initialize EPBs above the geomagnetic equator (Nishioka et al., 2012; Huba & Krall, 2013). However, this mechanism is inconsistent with the early knowledge that an ENW can

enhance the field-line integrated Pedersen conductivity and then depress the appearance/development of EPBs (Maruyama, 1988; Krall et al., 2009). Moreover, the activated EPBs near midnight could be secondary structures evolving from the topside structures of those drift-type/developed EPBs under the local ionospheric and thermospheric conditions. It is thus particularly obscure for the role of an ENW in initializing EPBs. More studies are required to investigate the possible role of an ENW in developing EPBs near midnight.

In this paper, we investigate multi-source perturbations in the evolution of an EPB event observed by an all-sky airglow imager (ASAI) deployed in low latitude, China on a geomagnetically quiet night (Kp < 3; Sum (Kp) = 15^{-}). We found this event initially evolved from the bottom-type structures. The possible roles the AGW- and CSI played in the formation of these bottom-type structures were discussed. We also separately explained how the PRE and equatorward wind-inducing RTIs drove those bottom-type structures to further develop into bifurcated/plume-like structures that occurred at post-sunset and near midnight. In section 2, we briefly describe the instruments and the data. Section 3 presents the results and analyses of the event, followed by section 5 as summaries and conclusions.

2. Instruments and Data

In this study, data from multiple ground-based instruments are used, including one ASAI deployed at Daxing (Dax; 22.6 °N, 107.1 °E; dip latitude ~12.6 °N); one very high frequency (VHF) radar at Fuke (Fuk; 19.5 °N, 109.1 °E; dip latitude ~9.5 °N); eight digisondes at Sanya (SaY; 18.4 °N, 109.0 °E; dip latitude ~8.5 °N), Fuke, ShaoYang (ShY; 27.2 °N, 111.5 °E; dip latitude ~17.2 °N), JEJU (JJ; 33.4 °N, 126.3 °E; dip latitude ~23.4 °N), I-CHEON (IC; 37.1 °N, 127.5 °E; dip latitude ~27.1 °N), Beijing (BJ; 40.3 °N, 116.2 °E; dip latitude ~30.3 °N), Mohe (MH; 52.0 °N, 122.5 °E; dip latitude ~42.0 °N), and LEARMONTH (LM; 21.8 °S, 114.1 °E; dip latitude ~31.8 °S). Among these instruments, the Fuk and MH digisondes, and the Fuk VHF radar belong to the Chinese Meridian Project (Wang C, 2010). Here note that the JJ, IC, ShY, BJ, LM, and MH stations are at mid-latitudes, and the Fuk and Dax stations are at low-latitude; the LM is close to the magnetic conjugation point of the BJ station. The color pentagrams in Figure 1 present the locations of these digisonde instruments; the red-filled dot represents the location of Dax ASAI, and the black-filled circle represents the nearly 160 ° field of view (FOV) of the Dax ASAI; the black-dotted line represents the magnetic equator (MQ).

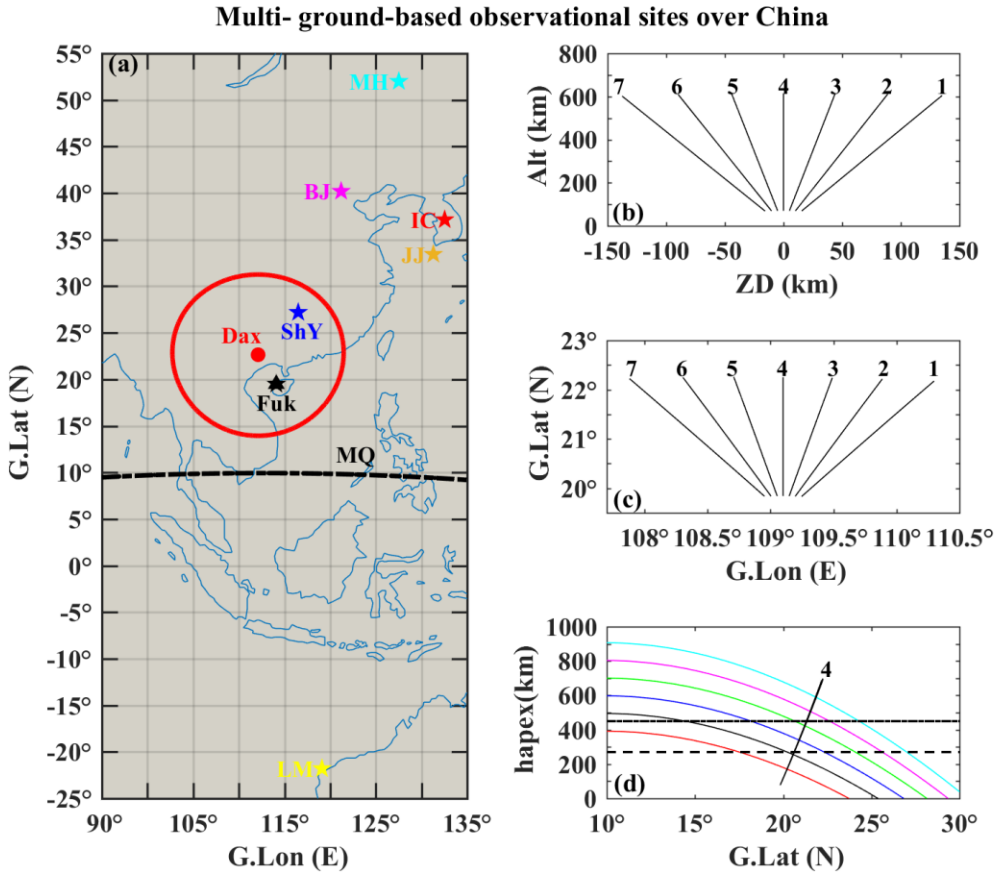

Figure 1. (a) Geographic locations of the ground-based instruments. (b)-(c) indicate the altitude-zonal and latitude-longitude distributions of the seven beams of the VHF radar. (d) hapex-latitude distributions of magnetic field lines at seven latitudes.

The Dax ASAI was constructed and installed by the State Key Laboratory of Space Weather, National Space Science Center (NSSC), Chinese Academy of Sciences (CAS) on 01 November 2011 (01-Nov-2011). The imager uses a Mamiya 24 mm/f4.0 fisheye lens with a 180 ° FOV. A filter with a bandwidth of 2.0 nm and a center wavelength of 630.0 nm is used. Using the method described by Garcia et al. (1997), we have eliminated distortion imposed by the fisheye lens to acquire Unwarped images. The perturbation (%) field airglow image δI was then obtained by $\delta I = (I - \bar{I})/\bar{I}$, where I and $\bar{I}$ are the intensity of an unwarped airglow image and a 1.0-h running mean of successive unwarped airglow images, respectively. Figure 2 presents the temporal evolution of an EPB event observed by the Dax ASAI on the night of 17 November 2015 (17-Nov-2015).

The Fuk VHF radar operates at a 47 MHz frequency with 54 kW peak power and a 2-MHz bandwidth to observe the 3.2 m scale FAIs by allocating the radar beams in directions perpendicular to the geomagnetic field lines. The detecting range of the radar is between 80 and 680 km. The minimum range resolution is 75 m. This radar uses an array composed of 4×8 Yagi antennas with 4.47 m spacing to form seven

(1-7) beams with a spacing of 7.5 °. Figures 1b-1c give the projected locations of the seven beams in the planes of geographic- altitude-zonal and latitude-longitude. The cone angle of each vertical beam is 21 °. Details about this radar can refer to the reference of Chen et al. (2017). Based on the same radar, Jin et al. (2021) statistically investigated the solar activity, season, and magnetic activity dependence of *F*-region 3.2-m scale field-aligned irregularities occurrence and vertical plasma drift over Fuk; Sun et al. (2021b) investigated the interaction of an EMSTID and an EPB that occurred over the equatorial ionization anomaly (EIA) crest region of China; Jin et al. (2022) recently investigated the interaction between postmidnight *F*-region irregularities and large-scale traveling ionospheric disturbances (LSTIDs) over China during geomagnetic disturbances. In this study, signal noise ratio (SNR) and the Doppler drift velocities recorded by this VHF radar are also used to investigate the vertical evolution of the passing-by EPB depletions.

Except for the ShY digisonde constructed by the Institute of Geology and Geophysics, Chinese Academy of Sciences (IGGCAS), the other seven digisondes used here are standard Digisonde Portable Sounder (DPS-4D; Reinisch et al., 2009). These digisondes routinely operate every 15 min to obtain an ionogram. During some equatorial spread *F* (ESF) seasons, the time resolution of an ionogram was adjusted to 7.5 min. By using the SAO software (https://ulcar.uml.edu/downloads.html), ionospheric parameters, including the virtual (peaked) height and critical frequencies of the *F2* layer [*h'f* (*hfp*) and *foF2*], were manually scaled from a mass of ionograms for the Fuk station. Scaled data of the *h'f* (*hfp*) and *foF2* from the SaY, JJ, IC, BJ, MH, and LM stations were downloaded from the Lowell GIRO Data Center (LGDC; https://giro.uml.edu/index.html). Some bad points of data were corrected by checking the corresponding ionograms. Scaled data of *h'f* (*hfp*) and *foF2* from the ShY station was provided by the IGGCAS (http://wdc.geophys.cn/). The time resolution is 1 hr. The height resolution of the *h'f* (*hfp*) for all stations is about 5 km. These ionospheric parameters [*h'f* (*hfp*) and *foF2*] were used to investigate the influences of the thermospheric meridional wind on the evolution of the EPB event. The simulated thermospheric wind from the horizontal wind mode (HWM-14; Drob et al., 2015) was also combined to explain the variations of the ionospheric parameters.

Besides the ground-based data above, the global vertical total electron content (VTEC) map data provided by the Navigation Headquarter of the Chinese Academy of Sciences (CAS-TEC map data) were also used to investigate the evolution of the EPB event. The time resolution for each map is 15 min. The height of the TEC is assumed at 450 km. Based on the database, Sun et al. (2020) investigated a WSA-like plasma patch, which affected the propagation/evolution of an EMSTID event over midlatitude, China; Sun et al. (2021b) further investigated the possible influence of EIAs on the propagation/evolution of an airglow event occurred over Dax, China.

3. Results and Analyses

3.1. Evolution of the EPB Event

Presented in Figure 2 are the processed airglow images on the EPB night. Figure 2a shows time sequences (in near 25 min intervals) of some unwarped images during 13:13:05-17:44:46 UT [university time; UT = LT (local time) + 7.14 in Dax]. Figure 2b gives the corresponding percentage perturbation (%) images. By assuming that the emission height of the airglow layer was 250 km, we have projected those unwarped/perturbation airglow images onto the uniformly geographic longitude-latitude region. The locations of the Fuk, Dax, and ShY stations were marked by black-filled triangles, red-filled circles, and blue-filled pentagrams respectively.

Here we first consider the temporal evolution of the EPB event. We suggest the reader skip Figure 2a and see Figure 2b since the sharper structures in Figure 2b make the reader well understandable the following description.

At 11:59:57 UT (the first image), the airglow depletion structure (d1) aligned with the geographic North-South (N-S) direction appeared in the southern FOV of the image. Its tip was passing through the head of the Fuk station (see the filled black triangle). Later, it proceeded to move poleward as it continuously drifted eastward, and gradually tilted westward. At 13:13:05 UT, it developed into a bifurcated structure when reaching a maximum poleward geographic latitude of about 27.0 °N. The mean poleward velocity of d1 was about 295 m/s (1062 km/hr). Later, the d1 became blurry, and its phase elongation again became aligned with the geographic N-S direction. After 15:39:32 UT, the d1 disappeared in the FOV of the images.

On the left of d1 is cluster-type depletions marked with the CDS1. Its scale is about 150 km. At 13:37:28 UT, the CDS1 appeared almost due south of the image. Like the d1, the CDS1 also continuously grew poleward as they drifted eastward. From 13:37:28 UT to 14:01:50 UT, the tip of the CDS1 hiked poleward about 1.2 ° (~140 km). The third depletion inside CDS1 (CDS1-3) extended to a maximum geographic latitude of about 21.5 °N. The mean poleward velocity of CDS1 reached about 97 m/s (350 km/hr). Interestingly, the CDS1 did not continue to grow poleward. Later 14:01:50 UT, it moved equatorward with a mean velocity of about 40 m/s (144 km/hr). After 16:52:49 UT, the CDS1 also fades out of the FOV of the images. Narayanan et al. (2016) first described this regressive characteristic of EPBs in latitudes as a shrinking phase of EPBs.

On the left of CDS1 is another cluster of depletions marked with CDS2. They had a slower growth that CDS1 when drifting eastward. From 14:01:50 UT to 15:15:03 UT, the third depletion inside CDS2 (CDS2-3) hiked poleward from about 24.7 °N to a maximum geographic latitude of 27.5 °N, with a mean poleward velocity of 73 m/s (262 km/hr). During the poleward growth of CDS2-3, a bifurcated structure evolved from the left wall of CDS2-3. After 15:15:03 UT, the CDS2-3 remained at its maximum poleward latitude (27.5 °N) until it finally drifted out of the FOV of the image.

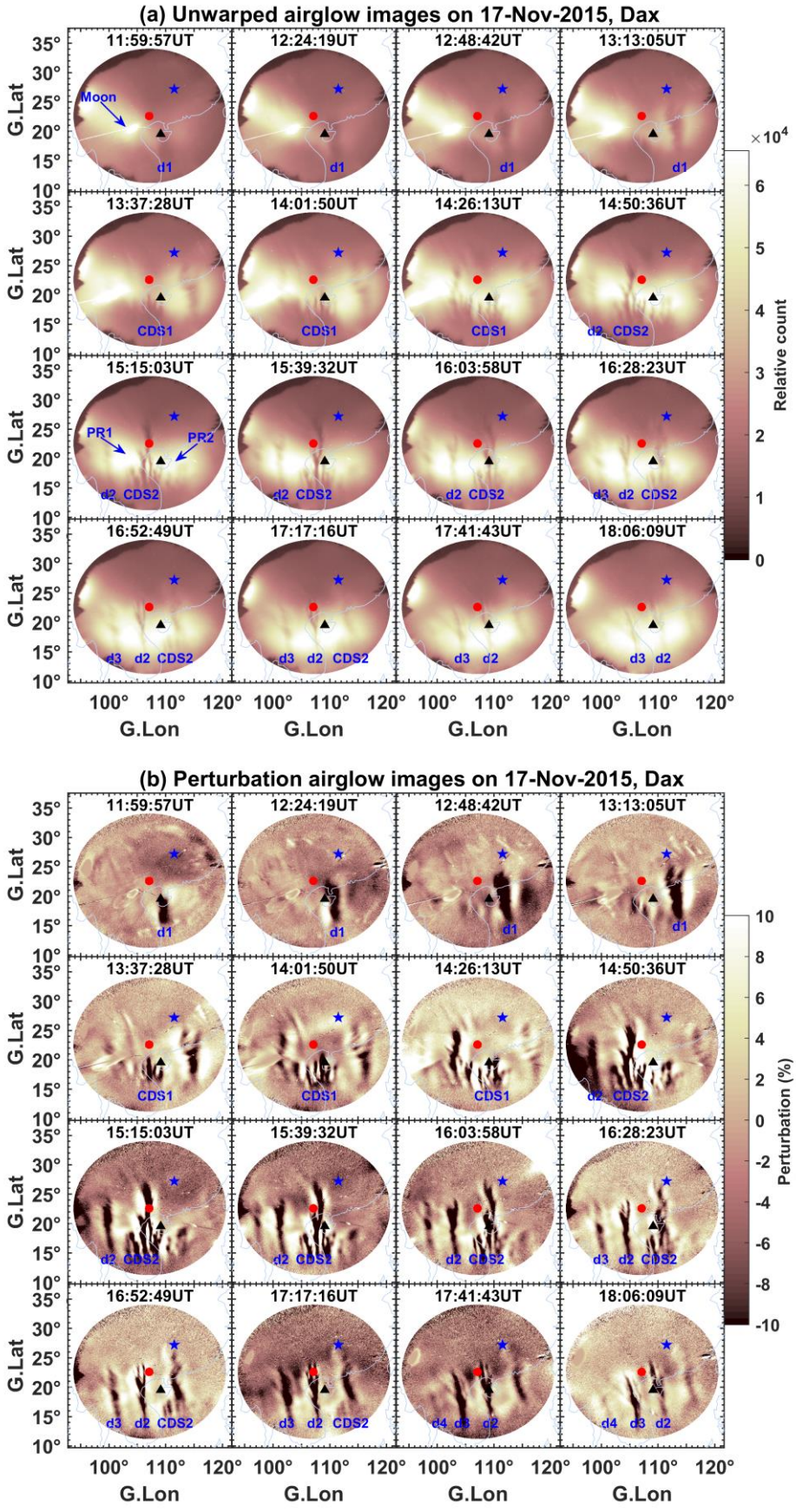

Figure 2. (a) Unwarped airglow images (in near 25 min intervals) on 17-Nov-2015. (b) the corresponding airglow perturbation images.

There are three depletions marked with d2-d4 subsequently appearing in the western regions of CDS2. Their wavefronts present the form of a plane wave. Although not so drastic in evolution as depletions d1 and CDS1-CDS2 described above, these depletions were still evolving and became bifurcation structures later.

There are other ionospheric phenomena appearing in Figure 2a. Firstly, a horizontal band-like region that has an extensional latitudinal width of near 5° and a broad longitudinal region appeared in the airglow images. As time proceeded, this region moved equatorward. Based on previous studies (e.g., Narayanan et al., 2013, 2014), this region is the EIA crest, which usually propagates equatorward at nighttime because of the so-called "antifountain effect." Secondly, two other patchy regions (marked with "PR1-PR2") with brighter airglow intensity appeared within the EIA region. Previous studies by Sun et al. (2017, 2021a) found this kind of brightness region is the true plasma phenomenon that has an enhanced plasma density than the surrounding ionosphere. These brightness structures were early called "blobs" by Pimenta et al. (2004, 2007).

Further presented in Figures 3-4 are the VHF radar observations to investigate the vertical evolution of those EPB depletions above. Figures 3a-3b show the UT variations of 3.2-m scale irregularities separately represented by the SNR and the Doppler shift velocities as the altitude. Figure 4 further gives the altitude-zonal distributions of the corresponding radar echoes. Radar echo structures resulting from the d1, CDS2-3, and d2 airglow structures were identified. Following are descriptions of the vertical evolution of these echo structures.

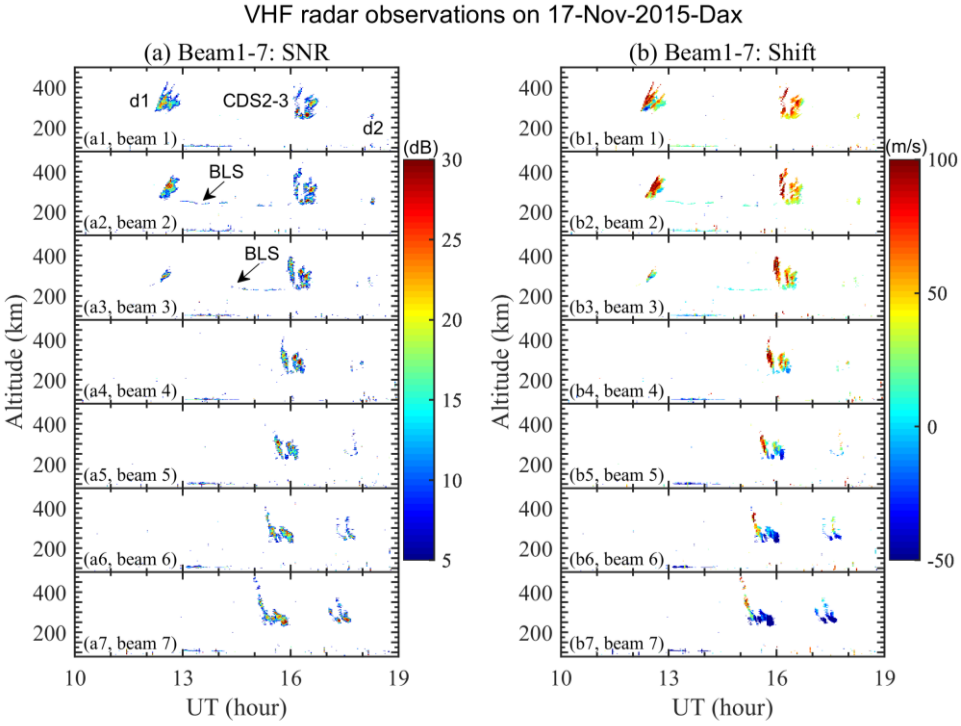

Figure 3. (a) SNR observed by beams 1-7 of the VHF radar on 17-Nov-2015. (b) the corresponding doppler shift. The radar echo structures of depletions d1-d2, and CDS2-3 were identified. The "BLS" presents the bottom-type layer structure.

From Figure 3a, beams 1-3 almost simultaneously detected the d1 echo structure at near 12:10 UT. The accompanied Doppler shift (positive upward) in Figures 3b1-3b3 exceeded 100 m/s. This upward movement of d1 can be also seen from the altitude-zonal distributions of the d1 echoes in Figure 4. Between 12:25 and 12:41 UT, the d1 extended upward from lower than 300 km to over 420 km. The vertical velocity was about 125 m/s (450 km/h). This estimated vertical velocity is near the maximum Doppler velocities along the radar beams.

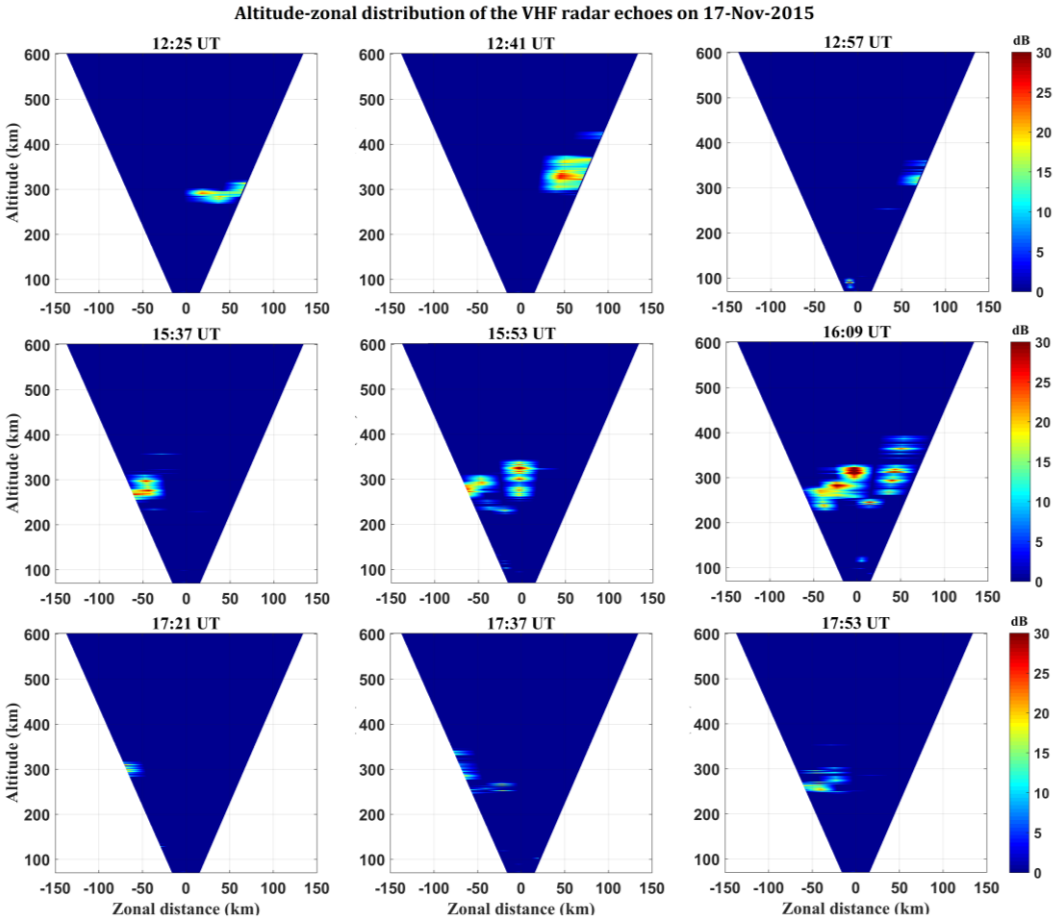

Figure 4. Altitude-zonal distribution of the radar echoes on 17-Nov-2015.

For the CDS2-3, its echo structure drifted eastward, consistent with the airglow observations. The westernmost beam 7 first detected the radar echoes near 15 UT, while beams 1-3 detected the radar echoes after midnight. Here note that the western beams 5-7 usually detected downward Doppler drift velocities, while the more eastern beams 1-4 detected upward ones. Returning to the airglow image at 16:03:58 UT in Figure 2b, one can see that a neck region of the bifurcated CDS2-3 was passing over the radar station (black-filled triangles; Fuk station). Because beams 1-3 (5-7) were directed to the left (right) branch of CDS2-3, one can infer that those radar echoes with upward (downward) Doppler drift velocities along the beams 1-3 (5-7) were

caused by the right (left) bifurcation of the CDS2-3. This result explains why only the right branch of CDS2-3 grew poleward, while the left one was almost no growth. Meanwhile, it means that the radar echoes detected by the beams 5-7 were caused by the secondary structures evolved from the topside structure of the developed depletions under the local ionospheric and thermospheric conditions. Of particular interest is that this bifurcated structure was also seen in the restructuring radar echo distribution in the altitude-zonal directions as presented in Figure 4. At 15:53 UT, the root of the neck of the bifurcation is at about 230 km. At 16:09 UT, the neck of the bifurcation was also elevated about 10 km; the mean upward vertical velocity of the neck is 10.4 m/s. During the same period, tips of the left/right branch of the CDS2-3 developed upward from 315/350 to 330/400 km, with a mean upward vertical velocity of 15.6/52 m/s. The estimated upward vertical velocity of CDS2-3 is thus less than one-half of the vertical velocity (about 125 m/s) of d1, just like the airglow observations did.

The VHF radar first detected the depletion d2 after 17 UT. Returning to Figure 2b, one can see that the d2 was passing by the head of the radar station at 17:17:16 UT. The d2 caused weaker Doppler echoes than the d1 and CDS2-3. The accompanied Doppler velocities in Figure 3b are downward. From the last three panels in Figure 4, one can see that after 17:21 UT the d2 echo was moving downward once it drifted into the FOV. The downward drift velocity is estimated at 35 m/s. This explains why after 17 UT the d2 airglow structure in Figure 2 stopped growing. Depletions appearing after 17 UT were classified into those so-called “fossilized bubbles” previously described by Chapagain (2015) and Sekar et al. (2007).

Worthy of that bottom-type layer structures (BLSs) were observed in Figure 3. From Figures 3a2-3a3, there are indications that these BLSs were connected with the roots of the plume-like echo structures d1 and CDS2. The accompanied Doppler drift velocities in Figures 3b2-3b3 were near 0 m/s.

3.2. Explanations of the EPB Evolution

Airglow and VHF radar observations described above present three kinds of depletions that occurred at sunset, near midnight, and post-midnight. Those depletions that occurred at sunset had a faster poleward/vertical velocity than those near- and post-midnight. To explain these differences, here we investigate the background ionospheric conditions during the evolution of all EPB depletions. Figures 5a2-5a3 give the temporary variations of the ionospheric height (*h'f*, *hfp*, and *hEs*), and *foF2* (*foEs*) from the Fuk digisonde on the EPB night. A time sequence of N-S cross-sections (keogram) of the successive airglow images in the Fuk longitude (109.1 ℃) was also shown in Figure 5a1. For a good comparison, the observed results on the night of 16/18-Nov-2015 were also presented in Figures 5b1-5b3 and 5c1-5c3.

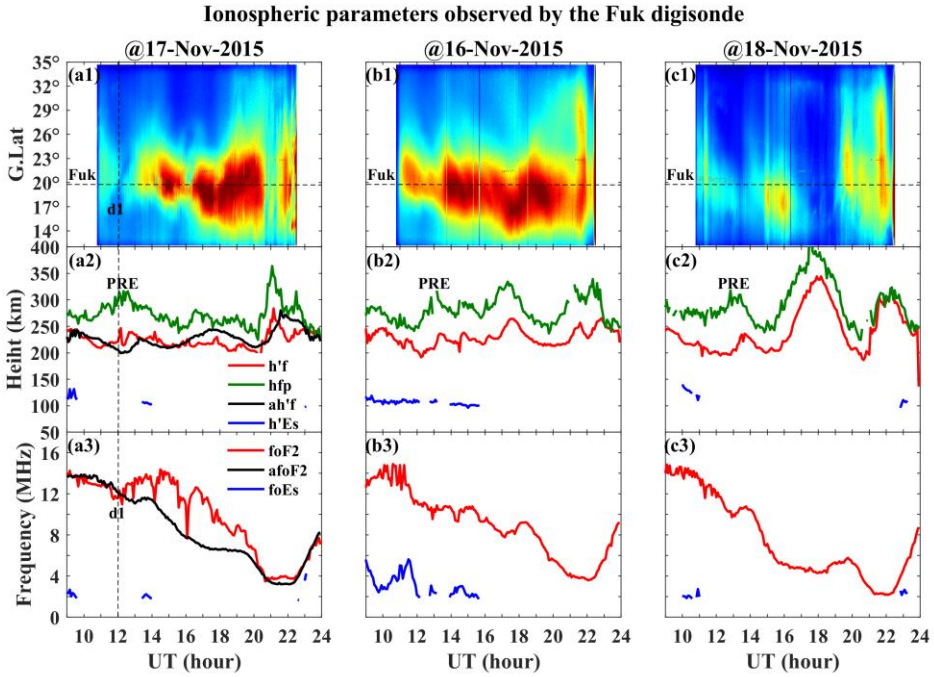

Figure 5. Ionospheric parameters observed by the Fuk digiosnde. (a) Results on 17-Nov-2015. (b) Results on 16-Nov-2015. (c) Results on 18-Nov-2015.

From Figure 5a2, between 11 and 13 UT, the ionospheric *h'f* (red line) had a slow increment of about 30 km during the poleward growth of d1. An elevation of about 50 km in the ionospheric *hfp* (green line) occurred almost simultaneously. A similar uplift also occurred slightly later on 16/18-Nov-2015. Such an uplift of the ionosphere at post-sunset is thus a true phenomenon. According to the previous studies by Fejer et al. (1991, 1999), this post-sunset ionospheric uplift resulted from the so-called PRE. Presented in Figure 6 is evidence more direct indicating the occurrence of such a PRE on this EPB night. Figure 6 shows the UT variations of the EIA crests as the geographic latitude along the Fuk longitude. One can see that between 12 and 13:50 UT the EIA crests moved poleward with a velocity of about 50 m/s. After 13:50 UT, the EIA reversed to equatorward with a velocity of about 75 m/s. The EIA's poleward/ equatorward movement was attributed to the inferred-PRE/antifountain-effect above. Interestingly, during the passage of the CDS2-3 (near 16 UT) no elevation occurred on the ionospheric bottomside. However, the passage of the CDS2-3 caused a small uplift in *hfp* (about 25 km) between 16 and 17 UT. Depletions d2-d4 did not cause any perturbations in both *h'f* and *hfp*. Between 14 and 20 UT, the bottomside ionosphere around Fuk remained almost horizontal, and the topside ionosphere varied a few. This explains why the observed EPB depletions survived through the night.

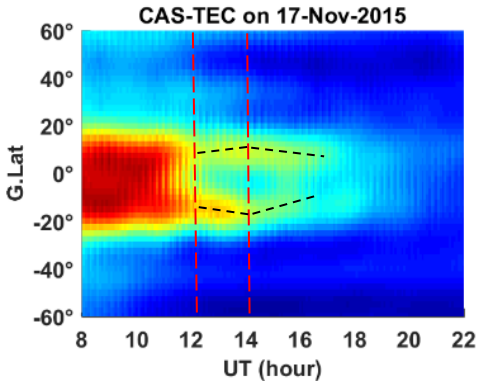

Figure 6. Geographic latitude-UT variations of the EIA crests reconstructed from the CAS-TEC map data on the night of 17-Nov-2015.

Variations of *foF2* are obvious during the EPB evolution. Passages of the d1 and CDS2-2 caused a decrement in *foF2* at near 12 and 16 UT. Moreover, there is a long time (near 8 hrs) increment in *foF2* when compared with the 10-day mean result (black-solid line) and those that occurred on 16/18-Nov-2015 (red-solid line). This result indicates that EPB depletions described above evolved in an ionospheric region filled with enhanced plasma.

Fejer et al. (1999) early found that the climatological occurrence of EPBs is well correlated with the post-sunset rise (PSSR) of the ionospheric *F* region caused by a PRE. At the sunset, the disappearance of the *E* region would result in an upward current that is not completely offset by the downward one driven by the *F* region dynamo. To close the current loops between *E* and *F* regions, a downward polarization electric field would be generated and pushed the EPBs drifting eastward with the almost same velocity as the background eastward wind (Haerendel et al., 1992). Because of the curl-free of downward electric field (Eccles, 1998; Eccles et al., 2015), an eastward-enhanced polarization electric field (PEF) would be generated on the daytime side of the solar terminator. This eastward-enhanced PEF is the PRE that is the most basic source for inducing the post-sunset EPBs, especially at equinoxes (Tsunoda, 1985).

What is the possible role the PRE played in the current case? As analyzed above, the uplift of the bottomside (peaked) ionosphere due to the PRE was about 30 (50) km within 2 hrs. If ignoring the photochemistry, the vertical upward mean velocity of the background ionosphere was about 5.5 m/s (19.8 km/hr). According to the IGRF-13 model (https://ccmc.gsfc.nasa.gov/modelweb/models/igrf_vitmo.php), the northward and downward components of the geomagnetic field (**B**) at 300 km above the Fuk station are ~0.034 and ~0.017 mT, respectively. If the estimated vertical upward velocity above was caused by the PRE, the background plasma would drift poleward at a velocity of about 11 m/s [5.5×(0.036/0.017) m/s]. This estimated poleward velocity for plasma is nearly a fifth of the inferred poleward velocity (~ 50 m/s) of the EIA before. This difference could be attributed to the height difference in digisonde

and GPS-TEC observations. The digisonde data estimated a PRE at the height between 250 and 300 km (from the bottomside to the peaked height of the ionosphere), while the GPS-TEC data estimated a PRE at the height of 450 km (topside ionosphere). A possible explanation is that the ionosphere below the peaked height located nearby/within the westward shear flow region of the bottomside ionosphere associated with the PRE (Kudeki & Bhattacharyya, 1998). The topside ionosphere is more sensitive than the bottomside ionosphere for the PRE on this EPB night. This is very reasonable because the plume-like echo structures of d1 and CDS2-3 were indeed connected with a bottom-type layer structure (BLS) on this event. Can such a low velocity cause the observed EPBs? From Figure 7 by Jin et al. (2022), there is about 5%-10% occurrence of ESF when the vertical drift velocity of the bottomside ionosphere reached 5-10 m/s. Besides, no EPBs occurred on 16/18-Nov-2015 when a comparable ionospheric uplift/PRE was observed. The main reason is that the PRE is not the only factor generating the bifurcated/plume-like structure of EPBs. Rather than the PRE, other seeding perturbations on the bottomside of the ionosphere also participate in the initiation of EPBs. When the bottomside structures were generated by the seeding perturbations, they would be further amplified by the PRE at the topside of the ionosphere.

Simulations conducted by Vadas (2007) verified that AGWs with a horizontal scale/wavelength higher than 150 km freely propagate in the thermosphere in the form of secondary waves. Makela et al. (2010) found that the distribution of spacings of EPBs at La Serena, Chile (geographic: 30.17°S, 289.19°E; geomagnetic: 16.72°S, 0.42°E) compares favorably to the spectrum of AGW-induced traveling ionospheric disturbances (TIDs) measured by Vadas & Crowley (2010) from a similar geographic latitude in the northern hemisphere. They found that the periodic spacing of EPBs could have a close relation to the properties of an underlying seed mechanism, namely the AGWs. Wu et al. (2017) reported an interesting EPB event in which the spacing of the successive two EPB depletions was equal to the wavelength of a circulated AGW caused by a typhoon. Based on the same ASAI, Sun et al. (2016) statistically found that most EPBs observed in the Chinese sectors occurred in groups of two to six depletions with an average spacing of ~200–300 km. All these results suggest the possible relationship between the spacings of EPBs and the AGWs. Returning to Figure 2, one can see that the d1, the primary structures of CDS1-CDS2, and the d2-d4 are successively ordered with a spacing of about 400 km along the longitude direction. AGWs with a wavelength of 400 km likely seeded the successive EPB depletions in the current event. The AGW seeding perturbations would result in bottom-type structures whose horizontal wavelength has the same spacing as the successive EPB depletions.

Vadas (2007) also pointed out that AGWs with a horizontal scale of less than 150 km would break and dissipate at the thermospheric height. Those cluster-like depletions inside CDS1/CDS2 on a smaller scale (~150 km) should evolve from other seeding perturbations. Hysell & Kudeki (2004) previously found that a collisional shear branch of the Kelvin Helmholtz instability (KHI) on the bottomside ionosphere can precondition the *F* region for initializing the bottom-type perturbations with an initial

wavelength of about 30 km and an asymptotic one of over 200 km. Simulation conducted by Aveiro & Hysell1 (2010) further verified that irregularity structures generated by the CSI were confined in the ionosphere bottomside when the gravity- and electric-field-driving RTIs were ignored. The bottom-type layer structures (BLSs) observed in the current event appeared at about 270 km, which corresponds to an apex height of ~456 km above the geomagnetic equator. Those cluster-type depletions with smaller-scale (~150 km) inside CDS2 in Figure 2 were confined very nearby 20° geographic latitude, which also corresponds to an apex height of ~456 km. Those cluster-type depletions in Figure 2 thus initially appeared at the same height as the bottom-type layer structure. The CSI mechanism is thus a very likely candidate to initiate the seeding perturbations of those smaller-scale depletions inside the CDS1-CDS2.

How did the seeding perturbations discussed above develop into the bifurcated/plume-like structures of EPB depletions? Beneath the d1 and CDS2-3 echoes in Figures 3a2-3a3 are regions connecting with a bottom-type layer structure observed by the VHF radar. The morphology of the d1 and CDS2-3 radar echo structures is very similar to those of plume-like structures that evolved from bottom-type layer structures in Figure 1 by Takahashi et al. (2010). Also, Hysell & Burcham, (1998) and Hysell (2000) found that different types of irregularities observed at Jicamarca usually occur sequentially, preceded by the occurrence of a bottom-type irregularity layer. The bottom-type irregularity layer was generally thought to be a precursor of a fully developed equatorial plasma plume (Hysell & Burcham, 2002; Li et al., 2017). Therefore, here we suggest that those AGW- and CSI- seeding perturbations described above could cause the bottom-type structures in the form of the wave-like and cluster-type depletions, which further evolved into the bifurcated/plume-like structures at the ionospheric topside.

So far, we have considered those EPB depletions in Figure 2 evolved from the bottom-type structures. However, one question remains: why did d1 depletion that first entered the FOV of the airglow images had a faster poleward/upward velocity than d2-d4/CDS2-3? Because the rapid poleward growth of the d1 occurred in a post-sunset elevated ionospheric region, bottomside structures of the d1 depletion could have been directly uplifted by the PRE and rapidly developed into bifurcated/plume-like structures at the ionospheric topside by the PRE-driving RTI process. However, this PRE-driving RTI mechanism is not sufficient to explain the d2-d4/CDS2-3 around midnight. Returning to Figure 2, one can see that when the d2-d4/CDS2-3 were/was evolving when the d1 had stopped growth. Meanwhile, from Figures 5a-5b and Figure 6, one can see that poleward growth of the d2-d4/CDS2-3 initialized when the antifountain effect began (~14 UT). This means that the PRE had almost uncoupled with the background ionosphere later 14 UT when the d2-d4/CDS2-3 appeared in the FOV of airglow images; the d2-d4/CDS2-3 were/was developing when the PRE had reversed to a westward electric field (WEF). Since a WEF would confine EPBs to the ionospheric bottomside and depress the EPB development (Seker et al. 2007), it is thus impossible for an electric field-driving RTI process to initialize the d2-d4/CDS2-3 later 14 UT. If no other physical processes, the

d2-d4/CDS2-3 later 14 UT should also stop growth as d1 did. An additional perturbation source is required to initialize the poleward growth of d2-d4/CDS2-3 again. This driving source is not as effective as the PRE-driving source.

Where did such a perturbation come from? Firstly, it is impossible for such a perturbation generated at a latitude lower than the Fuk station. If yes, when it propagated above the Fuk, the bottomside ionosphere around Fuk must be first elevated. However, the bottomside *h'f* around Fuk remained near 225 km between 14 and 16 UT while the CDS2 was persistently growing poleward. Therefore, it must be a perturbation that came from the latitudes higher than the Fuk station and persistently disturb the ionospheric topside. Here we can think of two possible perturbation sources: one is the polarization electric field generated by other ionospheric phenomena (e.g., *Es*) whose footprint connects with the topside region of Fuk station by the magnetic field line at the more northern latitude of Fuk; another is a nighttime neutral wind which blows equatorward from a higher latitude than the Fuk. We checked and excluded the strong *E*s activities (*foEs*> 5 MHz) that occurred in the ionograms from the more northern digisondes (e.g., ShY, IC, JJ, and BJ), since only very weak *Es* (*foEs*< 3 MHz) activities occasionally appeared on this night. However, an equatorward wind prevails at night, and can persistently elevate the ionosphere for a long time. It is possible that an equatorward wind as a sustaining source of instability to excite the generalized RTI at the topside ionosphere exceeding over several hours. Unfortunately, we have no usable neutral wind data on the EPB night. However, alternatively, we can use the height variations of the ionosphere at mid-latitudes to reflect the influence of neutral wind from the higher latitudes. This is very reasonable because the *F*-region dynamo generated at midlatitude is too much higher than those generated by the *E*-region dynamo (Richmond et al. 1980). Following is the simple deduction of such a wind.

To verify this possibility, Figures 7a1-7a6 and 7a8 present the ionospheric variations of *h'f* obtained from a digisonde chain that spanned from the SaY to the MH stations. The result indicates a significant uplift of the ionospheric *h'f* occurred during 12-16 UT at IC, JJ, BJ, and MH stations. The uplifts that occurred at mid-latitudes can be directly attributed to a nighttime equatorward wind. Two uplifts occurred at ShY station. The first uplift that occurred between 12 and 13 UT resulted from the same PRE observed by the Fuk/SaY digisonde. The uplift that occurred between 14 and 18 UT was attributed to the same equatorward wind observed at IC, JJ, BJ, and MH stations. However, at the same time, the equatorward wind did not cause any ionospheric perturbations at Fuk and SaY stations. Such an equatorward wind appeared in the mean wind (black-solid line) at postmidnight but disappeared on the EPB night. As will be analyzed later, the disappearance of such an equatorward wind at postmidnight at Fuk/SaY station was most likely offset by a poleward wind associated with a passing-by nighttime temperature maximum (TM; Colerico & Mendillo, 2002) from the lower latitudes. Sun et al. (2021a) previously verified such a poleward wind by analyzing relative variations between the ionospheric heights observed by a chain of digisondes and the meridional winds measured by a Fabry-Perot interferometer in the Chinese sectors. Note that a significant uplift

between 13 and 17 UT also occurred at LM station, which is located nearby the magnetic conjugation point of the BJ station. However, the uplift at BJ is higher than at LM. This suggests that the equatorward wind in the northern hemisphere was higher than in the opposite hemisphere during this time.

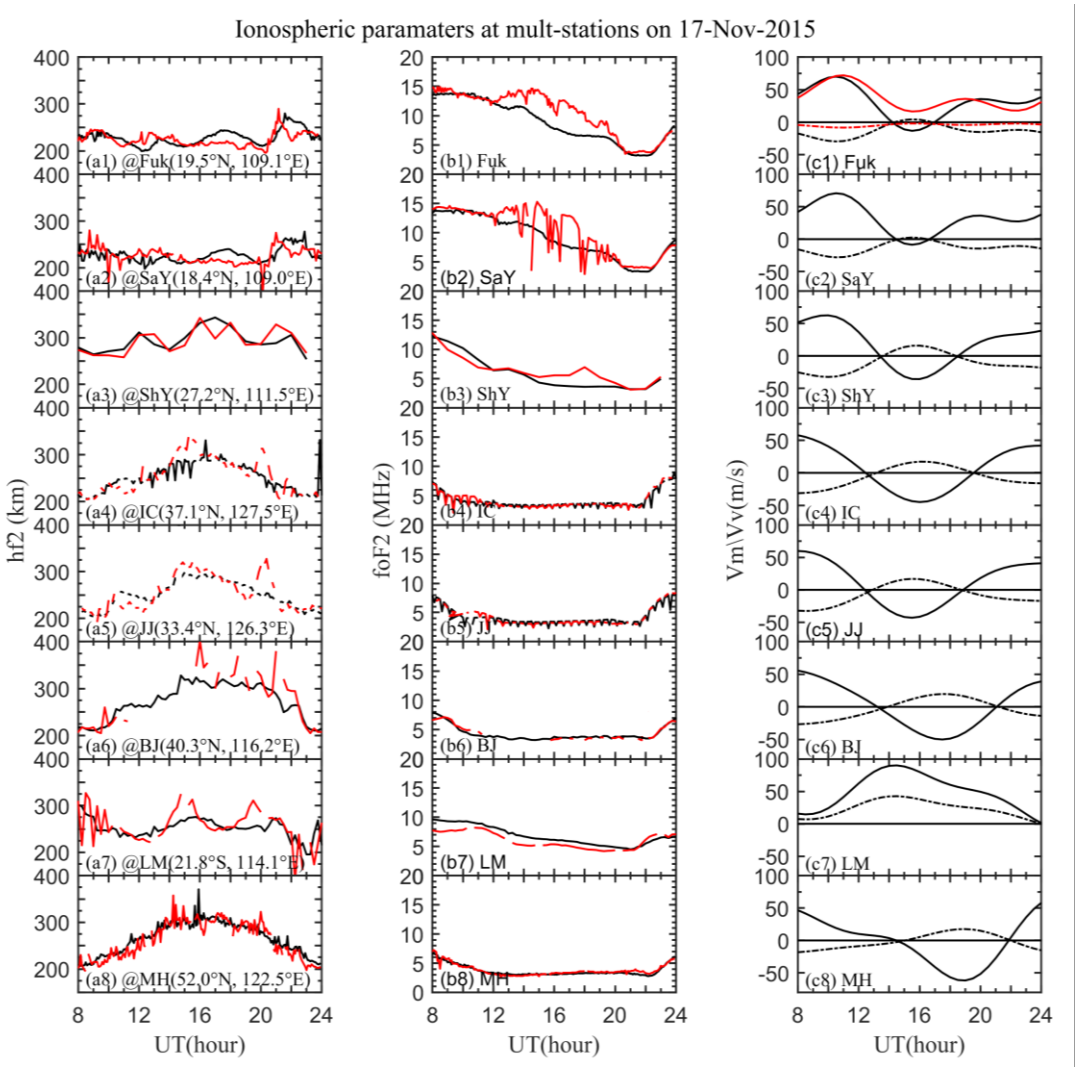

Figure 7. Ionospheric parameters at mult-stations on 17-Nov-2015. (a1-a8) present the ionospheric $h'f$ on 17-Nov-2015 (red-solid line) and the 10-day mean result (black-solid line) at eight digisonde stations. (b1-b8) give the corresponding *foF2*. (c1-c8) give the HWM-14 simulated meridional wind (250 km) and the corresponding vertical drift of plasma (dotted line; positive upward) caused by the HWM-14 simulated wind at the geographic locations of the eight digisondes.

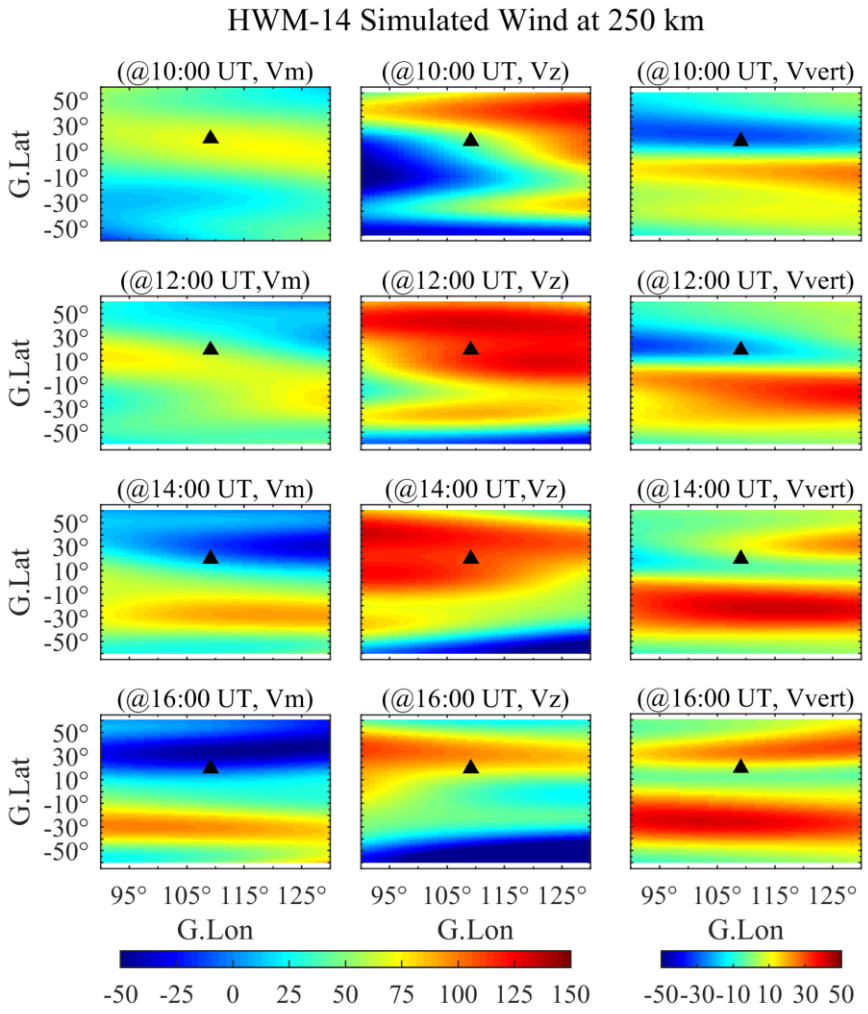

Figure 8. The HWM-14 simulated neutral wind at 250 km. The first column gives the meridional winds at 10, 12, 14, and 16 UT. The second column gives the corresponding zonal winds. The third column gives the calculated vertical plasma drift from the simulated meridional and zonal winds. The filled black triangle represents the location of Fuk.

Besides, we found that the HWM-14 model successfully captured such an equatorward wind on the EPB night. The main reason is that the HWM-14 model predicts a morphological neutral wind based on the statistical average of multi-data from the satellite and ground-based observations (Drob et al. 2015). It, therefore, can well reflect the daily and seasonal variations of the background neutral winds. Figures 7c1-7c8 give the simulated meridional winds at the geographic locations of those digisondes indicated in Figures 7a1-7a8. Figure 8 further presents the latitude-longitude distributions of the HWM-14 simulated meridional/zonal winds at 250 km. From Figure 7c (the black-solid line), an equatorward-enhanced neutral wind (positive equatorward/southward) first occurred near 12:30-13:30 UT for the BJ, JJ, IC, and ShY stations, and near 14:30 UT for the Fuk, SaY, and MH stations. It is visualized when the reader sees those meridional winds presented in the left column of Figure 8. At 14 UT a blue region presents the equatorward-enhanced wind already

propagated southward nearby the Fuk station (presented by the filled red pentagram). Amplitudes of the equatorward-enhanced wind gradually decreased as it propagated to lower latitudes. A possible reason is that the equatorward enhanced wind would become damped when propagating to the EIA region where the significant increase of the ion drag effect (Shiokawa et al. 2002) would slow down the passing-by neutral wind. Those dotted lines presented in Figures 7c1-7c8 further give the corresponding vertical drifts of plasma (positive upward) calculated by the HWM-14 simulated neutral wind. In the calculation, we included both the meridional and zonal winds and considered two factors of inclination and declination of the geomagnetic field lines at the height of 250 km. The same processes were conducted in calculating the latitude-longitude distributions of the vertical plasma drift as presented in the third column of Figure 8. The result indicates that a plasma jet with a vertical upward velocity of 10-30 m/s was passing nearby the Fuk station after 14 UT. Such an upward jet of plasma would result in the uplift of the bottomside ionosphere observed by those digisondes at mid-latitudes. However, as presented in Figures 7c1-7c2 (black dotted lines), the vertical drifts caused by the equatorward-enhanced neutral winds at Fuk and SaY stations are near 0 m/s. This well explains why the observed bottomside ionosphere remained almost horizontal between 14 and 16 UT at Fuk and SaY stations.

Based on the observations and the model results above, we found a vertical upward perturbation source of the plasma jet occurring in the northern region of the Fuk station. Such a perturbation source elevated the ionosphere and then resulted in those plume-like structures of d2-d4/CDS2-3 around midnight.

How did an equatorward wind trigger the plume-like structures of d2-d4/CDS2-3? Previous studies (e.g., Nishioka et al., 2012; Huba & Krall, 2013) suggested that the uplift of the ionosphere by an equatorward-enhanced wind could cause a decreasing ion-neutral collision frequency, resulting in an increasing gravity-driven eastward electric current that can initialize EPBs above the geomagnetic equator. This mechanism explains that those bifurcated/plume-like structures near midnight were generated from the bottomside of the ionosphere by the gravity-driven RTI process occurring above the magnetic equator. However, as analyzed in section 3.1, those plume-like structures of d2-d4/CDS2-3 only evolved from the topside structures of the developed depletions that extended over poleward 24°N later 14 UT. No elevation in *h'f* occurred around the Fuk when the d2-d4/CDS2-3 were/was growing poleward of the Fuk latitude. Those plume-like structures of d2-d4/CDS2-3 did not need to develop from the geomagnetic equator as the d1 did. Those plume-like structures of d2-d4/CDS2-3 found here were only the secondary structures that evolved from tips of the developed depletions at a latitude away from 10° (20°) the geomagnetic (geographic) equator by the equatorward wind-inducing generalized RTI process. Since the equatorward wind at low-mid latitudes usually reaches a maximum near midnight in our observations, it is expected that the maximum occurrence of the bifurcated/plume-like structures also appears near midnight. The equatorward wind-inducing RTI process described here should be the universal mechanism for triggering those activated EPB depletions/irregularities that occurred around midnight.

Since those secondary structures occurring around midnight did not directly evolve from the ionospheric bottomside, the equatorward wind-inducing RTI near midnight is not as effective as the PRE-driving RTI at sunset. This can reasonably explain why the d2-d4/CDS2-3 occurring near-midnight/at-postmidnight had slower growth than the d1 that occurred at post-sunset.

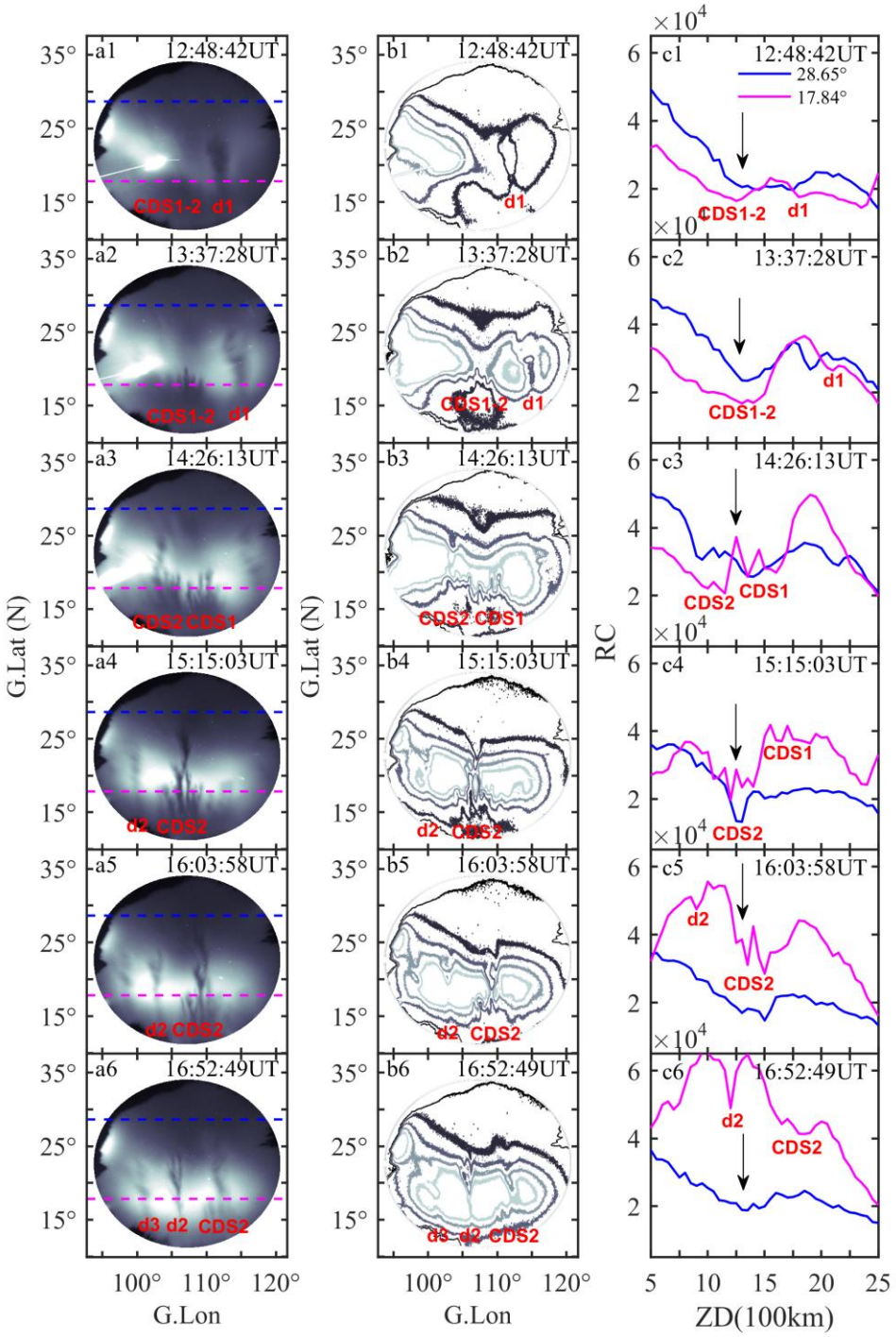

Figure 9. Airglow intensity counts scanned along the 17.84 ℃N and 28.65 ℃N geographic latitudes.

Besides, we found a large-scale wave structure (LSWS) could also participate in the evolution of the EPB event. Returning to Figure 2, one can find that at 14:26:13 UT CDS1 began to shrink equatorward when the CDS2 were evolving poleward. Why did CDS1 not follow the poleward growth of CDS2 after 14:26:16 UT? The main reason is that CDS1 and CDS2 were modulated by the anti-phase regions of an LSWS occurring on the ionospheric bottomside. To illustrate this, Figures 9c1-9c6 present variations of the relative airglow intensity counts along two selected latitudes (17.84 ° and 28.65 °N) in the airglow images indicated by the blue and magenta dotted lines in Figures 9a1-9a6. Presented in Figures 9c1-9c6 is a large-scale depleted region of airglow intensity with a width of near 600 km in the two curves of airglow intensity counts. This large-scale depletion of airglow intensity was caused by the upwelling region of an LSWS hiding in the airglow images. To visualize this upwelling region, Figures 9b1-9b6 present the contour lines of the airglow images. An upwelling region beneath plume-like structures of CDS1-2 located nearby the 105 °-110 °E longitude can be visualized at 13:37:28 UT. But later, the right CDS1 was gradually modulated into a trough/decreasing region of the LSWS. At 15:15:03 UT, the CDS1 was almost filled by the high plasma region that corresponds to the decreasing region of the LSWS. This could well explain why when CDS2 was evolving poleward CDS1 was shrinking equatorward.

What caused the LSWS found here? Simulation previously performed by Yokoyama et al. (2019) found that a vertical wind of 5 m/s caused by gravity can form an upwelling region, which penetrates the topside *F* region to be accelerated by the RTI process. It is enough for a vertical velocity perturbation of 5.5 m/s caused by the PRE reported here to cause an upwelling region from the bottomside ionosphere. However, from Figures 9c1-96, an LSWS also occurred at a latitude far away from the poleward tips of the depletions. Moreover, this LSWS occurred through the nighttime. These results could suggest that the LSWS is the coherent character of the background ionosphere. We suggest that the LSWS found here resulted from other physical processes rather than the PRE occurring at sunset; the LSWS could only participate in modulating the poleward development of the EPB depletions. An eastward/westward polarization electric field inside the upwelling/trough region of the LSWS could accelerate/suppress the development of the CDS2/CDS1.

A longtime plasma density enhancement occurred during 12-20 UT when the EPB depletions were evolving. It is a routine phenomenon that frequently occurs at low- and mid-latitudes. The morphology of the plasma density enhancement presented here is very similar to the one in Figure 7 by Sun et al. (2021b) observed by the same digisonde. This plasma density enhancement is a necessary condition for triggering the generalized RTI. What mechanisms resulted in such a plasma density enhancement? Sun et al. (2021b) previously explained this kind of plasma density enhancement as a combined result of a westward electric field (WEF) and a poleward-enhanced wind associated with a temperature maximum (TM) that occurred over the geomagnetic equator. Whether or not such a mechanism applies here. As analyzed in section 3, the EIA persistently moved equatorward between 14 and 18 UT because of the antifountain effect caused by a WEF. The WEF can compress the

plasma at higher altitudes to the ionospheric bottomside, causing a part of plasma density enhancement presented in Figure 5a3 or Figures 7b1-7b2. What is the possible role a TM played in the current event? Returning to Figure 5b or Figure 7a1, one can see that disappearance of uplift in *h'f* (red-solid line) occurred between 16 and 20 UT on the EPB night when compared with that of the 10-day mean result (black-solid line). It is reasonable for attributing the disappearance of such an uplift to a passing-by poleward wind associated with a TM from the geomagnetic equator. From Figure 5a1, a poleward reversal of the EIA began to occur at about 18 UT. A sudden decrement of about 25 km in *h'f* almost simultaneously occurred at 18 UT. However, accompanied by such a decrement of *h'f* is only a small hump in *foF2*. This suggests to us that the plasma density enhancement caused by the passage of a TM was not so prominent in the current case. The observed plasma density enhancement was mainly caused by the equatorward/downward compression of plasma in the bottomside ionosphere by a WEF. Why the plasma density enhancement persisted over 8 hrs? We suggest that the bottomside ionosphere provided a relatively stable condition occurring to prevent the erosion of the plasma because of the photochemical processes on this night. More plasma was accumulated on the bottomside of the ionosphere and caused the longtime plasma density enhancement.

4. Summaries and Conclusions

In this paper, we present the multi-source perturbations in the evolution of an equatorial plasma bubble (EPB) event observed by an all-sky airglow imager (ASAI) deployed at Dax (22.6 °N, 107.1 °E; dip latitude ~12.6 °N), China, on the night of 17 November 2015 (17-Nov-2015). A very high frequency (VHF) radar at Fuk (19.5 °N, 109.1 °E; dip latitude ~9.5 °N), and a ground-based chain of digisondes spanned the latitude from Sanyan (18.4 °N, 109.0 °E; dip latitude ~8.5 °N) to Mohe (52.0 °N, 122.5 °E; dip latitude ~42.0 °N) were combined to investigate the background ionospheric and thermospheric conditions that affected the evolution of the EPB event.

Observations indicated:

1. The primary structures of the EPB depletions were successively ordered with a spacing of about 400 km along the longitude direction; two cluster-type structures around the primary EPB depletions had a smaller spacing of ~150 km;
2. Three kinds of depletions that occurred near sunset, near midnight, and post-midnight were observed; those depletions occurring at sunset had a faster poleward/vertical velocity than those that occurred around midnight. Depletions that occurred at postmidnight became fossilized bubbles;
3. Accompanied by the EPB depletions are bottom-type layer structures that were connected to the roots of the plume-like irregularities observed by the VHF radar;
4. The poleward growth of those post-sunset depletions occurred when the

ionosphere was elevated by a prereversal enhancement of the zonal electric field (PRE); the relatively slower poleward growth of those near-midnight depletions occurred when an equatorward seasonal wind elevated the ionosphere in regions with a latitude higher than the geographic (geomagnetic) equator ~20 °(10 °);

Analyses indicated:

1. The EPB event evolved from the bottom-type structures that could be seeded by the AGW and CSI –inducing perturbations; the AGW with the same horizontal wavelength as the successive EPB depletions could explain the periodic characteristic of the EPB event; CSI occurring on the ionospheric bottomside could cause those cluster-type depletions on a smaller scale (~100-150 km);
2. The generalized RTI processes further drove those AGW and CSI –inducing bottom-type structures to form bifurcated/plume-like structures at the ionospheric topside: those plume-like depletions with faster growth at post-sunset evolved from the bottom-type structure most likely driven by the PRE-inducing RTI process; those near-midnight plume-like depletions with a slower poleward/upward velocity were the secondary structures evolved from topside structures of the developed depletions by a seasonal equatorward wind-inducing RTI process;
3. Those two cluster-type structures first appeared in the same upwelling region of a large-scale wave-like structure (LSWS), but later the right adjacent cluster-type structures were modulated into a rough/decreasing region of the LSWS. An eastward/westward polarization electric field inside the upwelling/trough region of the LSWS could accelerate/suppress the development of the left/right cluster-type depletions.

This paper thus highlights the significance of multi-source perturbations in the evolution of an EPB event that occurred over the low latitudes of China.

Data Availability Statement

The Mohe, Beijing, Shaoyan, and Sanya digisonde data was provided by the Institute of Geology and Geophysics, Chinese Academy of Sciences (IGGCAS; http://wdc.geophys.cn/) and supported in part by the Solar-Terrestrial Environment Research Network of CAS and Meridian Project of China. The manually scaled digisonde data from the Mohe, Beijing, Sanya, JEJU, I-CHEON, and LEARMONTH stations can be required from the Lowell GIRO Data Center (LGDC; https://giro.uml.edu/didbase/scaled.php). The raw LEARMONTH digisonde data were from the USAF NEXION Digisonde network, the NEXION Program Manager is Annette Parsons. The unwarped airglow data was uploaded to the National Space Science Data Center (NSSDC; http://cstr.cn/14804.11.sciencedb.00212). The digisonde and VHF radar data at Fuk were provided by the Chinese Meridian Project (http://data.meridianproject.ac.cn/en). The TEC map data provided by the Navigation

Headquarter of the Chinese Academy of Sciences (ftp://ftp.gipp.org.cn/product/ionex) were retrieved from the raw GPS/GLONASS data provided by NASA (https://cddis.nasa.gov/). The *Kp* data were provided by the World Data Center (WDC) (http://wdc.kugi.kyoto-u.ac.jp/wdc/Sec3.html).

Acknowledgments

This work was supported by the National Natural Science Foundation of China (Grants No. 41831073), the Youth Innovation Promotion Association of the Chinese Academy of Sciences (Grant No. 2020156), the Project of Stable Support for Youth Team in Basic Research Field, CAS (Grant No. YSBR-018), the National Key R&D Program of China (Grant No. 2021YFE0110200), and the International Partnership Program of the Chinese Academy of Sciences (Grant No. 183311KYSB20200003). We acknowledge the use of data from the Chinese Meridian Project, the CAS, the LGDC, the USAF NEXION Digisonde network, the WDC, and NASA.

References

Abdu, M. A., Batista, I. S., Takahashi, H., MacDougall, J., Sobral, J. H., Medeiros, A. F., and Trivedi, N. B. (2003). Magnetospheric disturbance induced equatorial plasma bubble development and dynamics: A case study in Brazilian sector. *J. Geophys. Res.*: *Space Phys.*, *108*(A12), 1449. https://doi.org/10.1029/2002JA009721

Abdu, M. A. (2012). Equatorial spread *F*/plasma bubble irregularities under storm time disturbance electric fields. *J. Atmos. Sol.-Terr. Phys.*, *75-76*, 44–56. https://doi.org/10.1016/j.jastp.2011.04.024

Ajith, K. K., Ram, S. T., Yamamoto, M., Otsuka, Y., & Niranjan, K. (2016). On the fresh development of equatorial plasma bubbles around the midnight hours of June solstice. *J. Geophys. Res.*: *Space Phys.*, *121*(9), 9051–9062. https://doi.org/10.1002/2016JA023024

Aveiro, H. C., & Hysell, D. L. (2010). Three-dimensional numerical simulation of equatorial *F* region plasma irregularities with bottomside shear flow. *J. Geophys. Res.*, *115*, A11321. https://doi.org/10.1029/2010JA015602

Burke, W. J., Huang, C. Y., Gentile, L. C., & Bauer, L. (2004). Seasonal-longitudinal variability of equatorial plasma bubbles. *Ann. Geophys.*, *22*, 3089–3098. https://doi.org/10.5194/angeo-22-3089-2004, 2004

Candido, C. M. N., Pimenta, A. A.， Bittencourt, J. A., & Becker-Guedes， F. (2008). Statistical analysis of the occurrence of medium-scale traveling ionospheric disturbances over Brazilian low latitudes using OI 630.0 nm emission all-sky images. *Geophys. Res. Lett.*, *35*, L17105. https://doi.org/10.1029/2008GL035043

Colerico, M. J., & Mendillo, M. (2002). The current state of investigations regarding

the thermospheric midnight temperature maximum (MTM). *J. Atmos. Sol.-Terr. Phys.*, *64*(12–14), 1361–1369. https://doi.org/10.1016/S1364-6826(02)00099-8

Chapagain, N. P. (2015). Dynamics ionospheric plasma bubbles measured by optical imaging system. *Journal of Institute of Science and Technology*, *20*(1), 20–27. https://doi.org/10.3126/jist.v20i1.13906

Chen, G., Jin, H., Yan, J.-Y., Cui, X., Zhang, S.-D., Yan, C.-X., et al. (2017). Hainan coherent scatter phased array radar (HCOPAR): System design and ionospheric irregularity observations. *IEEE Transactions on Geoscience and Remote Sensing*, *55*(8), 4757–4765. https://doi.org/10.1109/TGRS.2017.2699280

Dao, T., Otsuka, Y., Shiokawa, K., Ram, S. T., & Yamamoto, M. (2016). Altitude development of postmidnight *F* region field-aligned irregularities observed using Equatorial Atmosphere Radar in Indonesia. *Geophys. Res. Lett.*, *43*(3), 1015–1022. https://doi.org/10.1002/2015GL067432

Dao, T., Otsuka, Y., Shiokawa, K., Nishioka, M., Yamamoto, M., Buhari, S. M., Abdullah, M., & Husin, A. (2017). Coordinated observations of postmidnight irregularities and thermospheric neutral winds and temperatures at low latitudes. *J. Geophys. Res.*: *Space Phys.*, *122*(7), 7504–7518. https://doi.org/10.1002/2017JA024048

Drob, D. P., et al. (2015). An update to the Horizontal Wind Model (HWM): The quiet time thermosphere. *Earth and Space Science*, *2*, 301–319 https://doi.org/10.1002/2014EA000089

Eccles, J. V. (1998). Modeling investigation of the evening prereversal enhancement of the zonal electric field in the equatorial ionosphere. *J. Geophys. Res.*, *103*(A11), 26709–26719. https://doi.org/10.1029/98JA02656

Eccles, J. V., Maurice, J. P. St. & Schunk, R. W. (2015). Mechanisms underlying the prereversal enhancement of the vertical plasma drift in the low-latitude ionosphere. *J. Geophys. Res. Space Physics*, *120*, 4950–4970. https://10.1002/2014JA020664

Fejer, B. G., de Paula, E. R., González, S. A., & Woodman, R. F. (1991). Average vertical and zonal *F* region plasma drifts over Jicamarca. *Journal of Geophysical Research*, *96*(A8), 13901–13906. https://doi.org/10.1029/91JA01171

Fejer, B. G., Scherliess, L., & de Paula, E. R. (1999). Effects of the vertical plasma drift velocity on the generation and evolution of equatorial spread *F*. *J. Geophys. Res.*, *104*(A9), 19,859–19,869. https://doi.org/10.1029/1999JA900271

Garcia, F. J., Taylor, M. J., & Kelley, M. C. (1997). Two-dimensional spectral analysis of mesospheric airglow image data. *Appl. Opt.*, *36*(29), 7374–7385. https://doi.org/10.1364/AO.36.007374

Garcia, F. J., Kelley, M. C., Makela, J. J., & Huang, C.-S. (2000). Airglow observations of mesoscale low-velocity traveling ionospheric disturbances at midlatitudes. *Journal of Geophysical Research*, *105*(A8), 18407–18415.

https://doi.org/10.1029/1999JA000305

Haerendel, G., Eccles, J. V., & Çakir, S. (1992). Theory for modeling the equatorial evening ionosphere and the origin of the shear in the horizontal plasma flow. *J. Geophys. Res.*, *97*(A2), 1209–1223. https://doi.org/10.1029/91JA02226

Hysell, D. L., & Burcham, J. D. (1998). JULIA radar studies of equatorial spread *F*. *J. Geophys. Res.*, *103*(A12), 29, 155–29,167. https://doi.org/10.1029/98JA02655

Hysell, D. L. (2000). An overview and synthesis of plasma irregularities in equatorial spread. *J. Atmos. Sol. Terr. Phys.*, *62*(12), 1037–1056. https://doi.org/10.1016/s1364-6826(00)00095-x

Hysell, D. L., & Burcham, J. D. (2002). Long term studies of equatorial spread F using the JULIA radar at Jicamarca. *J. Atmos. Sol. Terr. Phys., 64*(12–14), 1531–1543. https://doi.org/10.1016/S1364-6826(02)00091-3

Hysell, D. L., & Kudeki, E. (2004). Collisional shear instability in the equatorial *F* region ionosphere. *J. Geophys. Res.*, *109*, A11301. https://doi.org/10.1029/2004JA010636

Huang, C. Y., Burke, W. J., Machuzak, J. S., Gentile, L. C., & Sultan, P. J. (2001). DMSP observations of equatorial plasma bubbles in the topside ionosphere near solar maximum. *J. Geophys. Res.*, *106*(A5), 8131–8142. https://doi.org/10.1029/2000JA000319

Huang, F., Dou, X., Lei, J., Lin, J., Ding, F., & Zhong, J. (2016). Statistical analysis of nighttime medium-scale traveling ionospheric disturbances using airglow imagers and GPS observations over central China. *Journal of Geophysical Research: Space Physics*, *121*, 8887–8899. https://doi.org/10.1002/2016JA022760

Huba, J. D., & Krall, J. (2013). Impact of meridional winds on equatorial spread *F*: Revisited. *Geophys. Res. Lett.*, *40*(7), 1268–1272. https://doi.org/10.1002/grl.50292

Jin, H., Zou, S., Yan, C., Yang, G., Chen, G., Zhang, S., et al. (2021). A statistical study of F-region 3.2-m-scale field-aligned irregularities occurrence and vertical plasma drift over Hainan: Solar activity, season and magnetic activity dependences. *Journal of Geophysical Research*: *Space Physics*, *126*, e2020JA028932. https://doi.org/10.1029/2020JA028932

Jin, H., Yan, C., Yang, G., Huang, F., Xie, H., Zhao, X., et al. (2022). Interaction between equatorial to low-latitude postmidnight *F*-region irregularities and LSTIDs in China during geomagnetic disturbances based on ground-based instruments. *Journal of Geophysical Research*: *Space Physics*, *127*, e2022JA030286. https://doi.org/10.1029/2022JA030286

Kelley, M. C. (1989). The Earth's ionosphere: Plasma physics and electrodynamics. In International Geophysics Series (Vol. 43). San Diego, CA: Academic Press. Retrieved from

https://library.isical.ac.in/cgi-bin/koha/opac-detail.pl?biblionumber=387710

Kelley, M. C., Makela, J. J., Ledvina, B. M., & Kintner, P. M. (2002). Observations of equatorial spread-*F* from Haleakala, Hawaii. *Geophysical Research Letters*, *29*(20), 2003–2011. https://doi.org/10.1029/2002GL01550

Krall, J., Huba, J. D., Joyce, G., and Zalesak, S. T. (2009). Three-dimensional simulation of equatorial spread-F with meridional wind effects. *Ann. Geophys.*, *27*(5), 1821–1830. https://doi.org/10.5194/angeo-27-1821-2009

Kudeki, E., & Bhattacharyya, S. (1999). Postsunset vortex in equatorial *F*-region plasma drifts and implications for bottomside spread-*F*. *J. Geophys. Res*., *104*(A12), 28163– 28170. https://doi.org/10.1029/1998JA900111

Li, G., Ning, B., Abdu, M. A., Wan, W., Wang, C., Yang, G., et al. (2017). First observation of presunset ionospheric F region bottom-type scattering layer. *Journal of Geophysical Research: Space Physics*, *122*, 3788–3797. https://doi.org/10.1002/2016JA023647

Makela, J. J., & Miller, E. S. (2008). Optical observations of the growth and day-to-day variability of equatorial plasma bubbles. *Journal of Geophysical Research*, *113*, A03307. https://doi.org/10.1029/2007JA012661

Makela, J. J., Vadas, S. L. Muryanto, R., Duly, T., & Crowley. G. (2010). Periodic spacing between consecutive equatorial plasma bubbles. *Geophys. Res. Lett*., *37*, L14103. https://doi.org/10.1029/2010GL043968

Martinis, C., Baumgardner, J. Wroten, J. & Mendillo, M. (2010). Seasonal dependence of MSTIDs obtained from 630.0 nm airglow imaging at Arecibo. *Geophys. Res. Lett*., *37*, L11103. https://doi.org/10.1029/2010GL043569

Maruyama, T. (1988). A diagnostic model for equatorial spread *F*, 1, Model description and application to electric field and neutral wind effects. *J. Geophys. Res.*: *Space Phys.*, *93*(A12), 14611–14622. https://doi.org/10.1029/JA093iA12p14611

Miller, E. S., Makela, J. J., & Kelley, M. C. (2009). Seeding of equatorial plasma depletions by polarization electric fields from middle latitudes: Experimental evidence. *Geophysical Research Letters*, *36*, L18105. https://doi.org/10.1029/2009GL039695

Narayanan, V. L., Taori, A., Patra, A. K., Emperumal, K., & Gurubaran, S. (2012). On the importance of wave-like structures in the occurrence of equatorial plasma bubbles: A case study. *Journal of Geophysical Research*, *117*, A01306. https://doi.org/10.1029/2011JA017054

Narayanan, V. L., Gurubaran, S., Emperumal, K., & Patil, P. T. (2013). A study on the night time equatorward movement of ionization anomaly using thermospheric airglow imaging technique. *J. Atmos. Sol.-Terr. Phys*., *103*, 113–120. https://doi.org/10.1016/j.jastp.2013.03.028

Narayanan, V. L., Shiokawa, K., Otsuka, Y., & Saito, S. (2014). Airglow observations

of nighttime medium-scale traveling ionospheric disturbances from Yonaguni: Statistical characteristics and low-latitude limit. *J. Geophys. Res.: Space Phys.*, *119*(11), 9268–9282. https://doi.org/10.1002/2014JA020368

Narayanan, V. L., Gurubaran, S., Shiokawa, K., & Emperumal, K. (2016). Shrinking equatorial plasma bubbles. *Journal of Geophysical Research: Space Physics*, *121*, 6924–6935. https://doi.org/10.1002/2016JA022633

Nishioka, M., Otsuka, Y., Shiokawa, K., Tsugawa, T., Effendy, Supnithi, P., Nagatsuma, T., & Murata, K. T. (2012). On post-midnight field-aligned irregularities observed with a 30.8-MHz radar at a low latitude: Comparison with *F*-layer altitude near the geomagnetic equator. *J. Geophys. Res.*: *Space Phys.*, *117*(A8), A08337. https://doi.org/10.1029/2012JA017692

Pimenta, A. A., Sahai, Y., Bittencourt, J. A., Abdu, M. A., Takahashi, H., & Taylor, M. J. (2004). Plasma blobs observed by ground-based optical and radio techniques in the Brazilian tropical sector. *Geophys. Res. Lett.*, *31*(12), L12810. https://doi.org/10.1029/2004GL020233

Pimenta, A. A., Sahai, Y., Bittencourt, J. A., & Rich, F. J. (2007). Ionospheric plasma blobs observed by OI 630 nm all-sky imaging in the Brazilian tropical sector during the major geomagnetic storm of April 6-7, 2000. *Geophys. Res. Lett.*, *34*(2), L02820. https://doi.org/10.1029/2006GL028529

Reinisch, B. W., Galkin, I. A., Khmyrov, G. M., Kozlov, A. V., Bibl, K., Lisysyan, I. A., et al. (2009). New Digisonde for research and monitoring applications. *Radio Science*, *44*, RS0A24. https://doi.org/10.1029/2008RS004115

Richmond, A. D., Blanc, M., Emery, B. A., Wand, R. H., Fejer, B. G., Woodman, R. F., et al. (1980). An empirical model of quiet-day ionospheric electric fields at middle and low latitudes. *Journal of Geophysical Research*, *85*(A9), 4658–4664. https://doi.org/10.1029/JA085iA09p04658

Shiokawa, K., Ihara, C., Otsuka, Y., & Ogawa, T. (2003). Statistical study of nighttime medium-scale traveling ionospheric disturbances using midlatitude airglow images. *Journal of Geophysical Research*, *108*(A1), 1052. https://doi.org/10.1029/2002JA009491

Shiokawa, K., Otsuka, Y., Ejiri, M. K., Sahai, Y., Kadota, T., Ihara, C., Ogawa, T., Igarashi, K., Miyazaki, S., & Saito, A. (2002). Imaging observations of the equatorward limit of midlatitude traveling ionospheric disturbances. *Earth Planets Space*, *54*, 57–62. https://doi.org/10.1186/BF03352421

Sekar, R., Chakrabarty, D., Sarkhel, S., Patra, A. K., Devasia, C. V., & Kelley, M. C. (2007). Identification of active fossil bubbles based on coordinated VHF radar and airglow measurements. *Annals of Geophysics*, *2*5, 2099–2102. https://doi.org/10.5194/angeo-25-2099-2007

Sun, L., Xu, J., Wang, W., Yuan, W., Li, Q., & Jiang, C. (2016). A statistical analysis of equatorial plasma bubble structures based on an all-sky airglow imager

network in China. *Journal of Geophysical Research: Space Physics*, *121*(11), 11495–11517. https://doi.org/10.1002/2016JA022950

Sun, L., Xu, J., Wang, W., Yuan, W., & Zhu, Y. (2017). Evolution processes of a group of equatorial plasma bubble (EPBs) simultaneously observed by ground-based and satellite measurements in the equatorial region of China. *J. Geophys. Res*., *Space Physics*, *122*, 4819–4836. https://doi.org/10.1002/2016JA023223

Sun, L., Xu, J., Zhu, Y., Yuan, W., Chen, Z., Hao, Y., et al (2020). Interaction between a southwestward propagating MSTID and a poleward moving WSA-like plasma patch on a magnetically quiet night at midlatitude China region. *Journal of Geophysical Research: Space Physics*, *125*, e2020JA028085. https://doi.org/10.1029/2020JA028085

Sun, L. C., Xu, J. Y., Zhu, Y. J., Yuan, W., & Zhao, X. K. (2021a). Case study of an Equatorial Plasma Bubble Event investigated by multiple ground-based instruments at low latitudes over China. *Earth Planet. Phys*., *5*(5), 1–15. http://doi.org/10.26464/epp2021048

Sun, L., Xu, J., Zhu, Y., Xiong, C., Yuan, W., Wu, K., et al. (2021b). Interaction between an EMSTID and an EPB in the EIA crest region over China. *Journal of Geophysical Research*: *Space Physics*, *126*, e2020JA029005. https://doi.org/10.1029/2020JA029005

Takahashi, H., Taylor, M. J., Pautet. P.-D., Medeiros, A. F., Gobbi, D., et al. (2009). Simultaneous observation of ionospheric plasma bubbles and mesospheric gravity waves during the SpreadFEx Campaign. *Ann. Geophys*., *27*, 1477–1487. https://doi.org/10.5194/angeo-27-1477-2009

Takahashi, H., et al. (2010), Equatorial ionosphere bottom-type spread *F* observed by OI 630.0 nm airglow imaging. *Geophys. Res. Lett*., *37*, L03102. https://doi.org/10.1029/2009GL041802

Thampi, S. V., Yamamoto, M., Tsunoda, R. T., Otsuka, Y., Tsugawa, T., Umemoto, J., & Ishii, M. (2009). First observations of large-scale wave structure and equatorial spread F using CERTO radio beacon on the C/NOFS satellite. *Geophysical Research Letters*, *36*, L18111. https://doi.org/10.1029/2009GL039887

Tsunoda, R. T., Livingston, R. C., McClure, J. P., & Hanson, W. B. (1982). Equatorial plasma bubbles: Vertically elongated wedges from the bottomside *F* layer. *Journal of Geophysical Research*, *87*(A11), 9171–9180. https://doi.org/10.1029/JA087iA11p09171

Tsunoda, R. T. (1985), Control of the seasonal and longitudinal occurrence of equatorial scintillations by the longitudinal gradient in integrated *E* region Pedersen conductivity. *J. Geophys. Res*., *90*, 447–456. https://doi.org/10.1029/JA090iA01p00447.

Tsunoda, R. T. (2005). On the enigma of day-to-day variability in equatorial spread *F*.

Geophysical Research Letters, *32*, L08103. https://doi.org/10.1029/2005GL022512

Tsunoda, R. T., Bubenik, D. M., Thampi, S. V., & Yamamoto, M. (2010). On large-scale wave structure and equatorial spread *F* without a post-sunset rise of the *F* layer. *Geophysical Research Letters*, *37*, L07105. https://doi.org/10.1029/2009GL042357

Vadas, S. L. (2007). Horizontal and vertical propagation and dissipation of gravity waves in the thermosphere from lower atmospheric and thermospheric sources. *Journal of Geophysical Research*, *112*, A06305. https://doi.org/10.1029/2006JA011845

Vadas, S. L., & Crowley, G. (2010). Sources of the traveling ionospheric disturbances observed by the ionospheric TIDDBIT sounder near Wallops Island on 30 October 2007. *J. Geophys. Res.*, *115*, A07324. https://doi.org/10.1029/2009JA015053

Wang, C. (2010). New chains of space weather monitoring stations in China. S*pace Weather*, *8*(8), S08001. https://doi.org/10.1029/2010SW000603

Weber, E. J., Brinton, H. C., Buchau, J., & Moore, J. G. (1982). Coordinated airborne and satellite measurements of equatorial plasma depletions. *Journal of Geophysical Research*, *87*(A12), 10503–10513. https://doi.org/10.1029/JA087iA12p10503

Wu, K., Xu, J. Y., Wang, W. B., Sun, L. C., Liu, X., & Yuan, W. (2017). Interesting equatorial plasma bubbles observed by all-sky imagers in the equatorial region of China. *J. Geophys. Res.*: *Space Phys.*, *122*(10), 10596–10611. https://doi.org/10.1002/2017JA024561

Wu，K., Xu，J. Y., Yue，X. A., Xiong，C., & Luo, L (2020). Equatorial plasma bubbles developing around sunrise observed by an all-sky imager and global navigation satellite system network during storm time. *Ann. Geophys.*, *38*, 163–177. https://doi.org/10.5194/angeo-38-163-2020

Xu, J., Li, Q., Sun, L., Liu, X., Yuan, W., Wang, W., Yue, J., Zhang, S., Liu, W., Jiang, G., Wu, K., Gao, H. & Lai, C. (2021). The Ground-Based Airglow Imager Network in China. In Upper Atmosphere Dynamics and Energetics (eds W. Wang, Y. Zhang and L.J. Paxton). https://doi.org/10.1002/9781119815631.ch19

Yokoyama, T., Yamamoto, M., Otsuka, Y., Nishioka, M., Tsugawa, T., Watanabe, S., & Pfaff, R. F. (2011). On postmidnight low-latitude ionospheric irregularities during solar minimum: 1. Equatorial Atmosphere Radar and GPS-TEC observations in Indonesia. *J. Geophys. Res.*: *Space Phys.*, *116*(A11), A11325. https://doi.org/10.1029/2011JA016797

Yokoyama, T., Jin, H., Shinagawa, H., & Liu, H. (2019). Seeding of equatorial plasma bubbles by vertical neutral wind. *Geophysical Research Letters*, *46*, 7088–7095. https://doi.org/10.1029/2019GL083629